ChemPubSoc Europe

DOI: 10.1002/cctc.201801299

CHEMCATCHEM Full Papers

Determination of Molybdenum Species Evolution during Non-Oxidative Dehydroaromatization of Methane and its Implications for Catalytic Performance

Miren Agote-Arán,[a, b] Anna B. Kroner,[b] Husn U. Islam,[c] Wojciech A. Sławiński,[d, e] David S. Wragg,[d] Inés Lezcano-González,*[a, f] and Andrew M. Beale*[a]

Mo/H-ZSM-5 has been studied using a combination of *operando* X-ray absorption spectroscopy and High Resolution Powder Diffraction in order to study the evolution of Mo species and their location within the zeolite pores. The results indicate that after calcination the majority of the species present are isolated Mo-oxo species, attached to the zeolite framework at the straight channels. During reaction, Mo is first partially carburized to intermediate MoC_xO_y species. At longer reaction times Mo fully carburizes detaching from the zeolite and aggregates forming initial $Mo_{1.6}C_3$ clusters; this is coincident with maximum benzene production. The $Mo_{1.6}C_3$ clusters are then observed to grow, predominantly on the outer zeolite surface and this appears to be the primary cause of catalyst deactivation. The deactivation is not only due to a decrease in the amount of active Mo surface but also due to a loss in shape-selectivity which leads to an increased carbon deposition at the outer shell of the zeolite crystals and eventually to pore blockage.

Introduction

As we move away from traditional sources of platform chemicals to more sustainable ones, processes for the conversion of methane will be required for both medium (i.e. through utilization of methane derived from shale gas and hydrates) and long-term (bio-genic sources) applications.[1] Presently methane is largely used for the production of syngas ($CO + H_2$), which is then upgraded to fuels or chemicals through technologies such as the Fischer-Tropsch process.[2] This route is energy intensive and expensive, so the development of direct processes is an important goal to reduce costs. Methane dehydroaromatization (MDA) is a promising reaction as it converts methane directly into aromatics and light hydrocarbons as well as a significant amount of H_2 as co-product.

The most widely studied catalyst for MDA is Mo/H-ZSM-5 zeolite,[3] typically prepared *via* ion exchange, leading to formation of Mo-oxo centers anchored at the Brønsted sites inside the zeolite pores. It is accepted that under MDA conditions, initial Mo-oxo species carburize resulting in active Mo centers which are responsible for transformation of methane into C_2 and C_3 hydrocarbon intermediates. Subsequently, these intermediates react on the Brønsted acid sites (BAS) and are transformed into aromatics, *via* a bifunctional mechanism involving the assistance of Mo species.[4,5] The pore dimensions of the H-ZSM-5 zeolite are believed to provide shape selectivity favoring benzene formation with up to 80% selectivity.[6]

Despite Mo/H-ZSM-5 presenting promising performance, its commercialization is compromised by the rapid deactivation during the MDA reaction due to the accumulation of carbon deposits.[2,4,6,7] There is ongoing debate regarding the nature and location of these deposits which have been reported to occur in the internal or external surface and have been associated to both, molybdenum centers and BAS sites.[8–13] For that matter, several

[a] M. Agote-Arán, Dr. I. Lezcano-González, Prof. A. M. Beale
Research Complex at Harwell
Rutherford Appleton Laboratory
Didcot OX11 0FA (UK) &
Chemistry Department, University College of London
20 Gordon Street, London, WC1H 0AJ (UK)
E-mail: i.lezcano-gonzalez@ucl.ac.uk
Andrew.Beale@ucl.ac.uk
[b] M. Agote-Arán, Dr. A. B. Kroner
Diamond Light Source Ltd.
Harwell Science and Innovation Campus
Didcot OX11 0DEU (UK)
[c] Dr. H. U. Islam
Johnson Matthey Technology Centre
Blount's Court
Sonning Common
Reading RG4 9NH (UK)
[d] Dr. W. A. Sławiński, Dr. D. S. Wragg
INGAP Centre for Research Based Innovation
Department of Chemistry
University of Oslo
N-0315 Oslo (Norway)
[e] Dr. W. A. Sławiński
The ISIS Facility
STFC Rutherford Appleton Laboratory
OX11 0QX (UK)
[f] Dr. I. Lezcano-González
UK Catalysis Hub
Research Complex at Harwell
Rutherford Appleton Laboratory
Didcot OX110FA (UK)

Supporting information for this article is available on the WWW under https://doi.org/10.1002/cctc.201801299

This manuscript is part of the Anniversary Issue in celebration of 10 years of ChemCatChem.

research groups have been investigating a number of approaches to overcome catalyst deactivation. These approaches include the use of zeolite structures with greater tolerance to carbon deposition (i.e. MCM-22),[12,14,15] the regeneration of deactivated catalysts with oxidants (e.g. O_2, CO_2), hydrogen or alkanes/alkenes feed, [5,16–21] and the integration of an ion-conducting membrane into the reactor.[22] Although encouraging progress has been made, catalyst deactivation is far from being overcome, and a better understanding is required for improved catalyst design.

Mo sintering under reaction conditions is also believed to contribute to catalyst deactivation;[9,23] in line with this, studies by Wachs et al.[24] point out the instability of Mo carbide clusters with C/Mo ratio >1.5 inside the zeolite channels, considering them prone to migrate to the zeolite outer surface. In spite of the extensive investigations on the nature of the active Mo species,[25–29] there is no consensus regarding the precise location and structure of active Mo sites,[10,23,28,30] and little is known about its impact on catalyst deactivation. Recent X-ray emission studies carried out by our group,[31] suggest that initial Mo-oxo species are first transformed to MoC_xO_y at the early stages of reaction (also known as the induction period). As the reaction proceeds, MoC_xO_y fully carburizes into a MoC_x-type phase and aromatization commences. It was hypothesized that this full carburization would lead to detachment of Mo species from zeolite ion-exchange positions, making them susceptible for sintering.

Clearly then, further insight into the structure and location of the evolving Mo species is needed to fully understand their role in catalytic performance and eventual deactivation. In this work we present *operando* X-ray Absorption Spectroscopy (XAS) (with product formation verified using mass spectrometry (MS)) studies in combination with separate high-resolution powder diffraction (HRPD) in order to understand the relationship between the nature and location of Mo species and catalytic performance. We note that, in particular, this insight has been achieved by applying *operando* X-ray absorption fine structure (EXAFS) spectra which are of sufficient quality to allow for obtaining detailed insight into the local structure of the Mo environment and also to correlate these structures with the catalytic performance; this is unlike many previous studies where data have been obtained on quenched samples and where there is always a risk that the quenching process could compromise the results obtained. Meanwhile, Rietveld refinement of the HRPD data and the accompanying Fourier difference analysis enabled us to locate Mo species within the zeolite channels and to observe how these species evolve. With this combined approach, we provide a unique and more complete understanding of the relationship between structure, location and catalyst function.

Results and Discussion

Catalyst Characterization

Mo/H-ZSM-5 is typically synthesized from a physical mixture of crystalline MoO_3 and H-ZSM-5 calcined at high temperature (i.e. 700 °C). The thermal treatment is known to lead to the migration of Mo into the zeolite channels, anchoring at the zeolite Brønsted acid sites.[25]

Table 1. Textural and physicochemical properties of the zeolite materials studied.

Sample	Carbon content [wt.%]	Mo content [wt.%]	S_{BET} [m^2/g]	V_{micro} [cm^3/g]
H-ZSM-5	–	–	412	0.15
MoO_3 + H-ZSM-5	–	3.72	385	0.15
Mo/H-ZSM-5 calcined	–	3.80	344	0.12
Mo/H-ZSM-5 7 min MDA	0.4	–	351	0.12
Mo/H-ZSM-5 25 min MDA	0.9	–	360	0.13
Mo/H-ZSM-5 90 min MDA	3.8	–	326	0.11

Mo loading obtained from chemical analysis and textural properties of these samples (surface area and micropore volume measured by N_2 physisorption) are presented in Table 1. The table also includes characterization of the catalyst at different reaction times (i.e. 7, 25 and 90 min of MDA reaction (50% CH_4/Ar; GHSV = 750 h^{-1}, 700 °C)) including carbon content quantified by thermogravimetric analysis, and surface areas and micropore volumes.

Mo loading for the catalyst before and after calcination is determined to be ~3.8 wt.%. The introduction of Mo into the H-ZSM-5 upon calcination is evidenced by the decrease in the zeolite micropore volume (18.7% decrease). For short reaction times, up to 25 min, the carbon content accumulated on the catalyst from MDA activity is rather low (up to 0.9 wt.% after 25 min of reaction); the drop in micropore volume to 0.11 cm^3/g for the sample reacted for 90 min suggests an increased presence of carbon deposits (3.8 wt.%) which may partially block or fill the zeolite pores.

The dispersion of Mo upon calcination was verified by X-ray diffraction (XRD) and Fourier transform infra-red (FTIR) shown in Figure S1 in the electronic supporting information (ESI). While the XRD pattern (Figure S1a) of the Mo-containing sample before calcination exhibits reflections of both MoO_3 and the zeolite, the diffraction peaks corresponding to MoO_3 crystals completely disappear in the calcined catalyst suggesting good metal dispersion.[32,33] By FTIR (Figure S1b) the intensity decrease of zeolite hydroxyl bands is observed upon calcination of MoO_3 and H-ZSM-5 physical mixture evidencing the anchoring of Mo to the zeolite.

Operando X-ray Absorption Spectroscopy

Mo K-edge XAS spectra of the as-prepared catalyst were collected during calcination (up to 700 °C, 20% O_2/He, 5 °C/min) as well as during subsequent MDA reaction (50% CH_4/Ar, GHSV = 3000 h^{-1}, 700 °C, 92 min). As previously reported, Mo K-edge XANES spectra showed a clear change in Mo environment upon calcination (Figure S2 in ESI); i.e. the metal was seen to evolve from an octahedral-like symmetry (corresponding to MoO_3 precursor) to a highly dispersed, isolated tetrahedra, as evidenced by an increased intensity of the pre-edge peak and a relatively featureless post-edge region.[26,34] Our data shows that on commencement of the

MDA reaction the Mo K-edge XANES spectra possess strong similarities to reference compounds containing tetrahedral 'monomeric' Mo^{VI}, suggesting these are the majority of species present in the catalyst. Note however that the presence of other Mo-containing species cannot be entirely ruled out.

The MS traces of the hydrocarbon products detected during the MDA reaction (T = 700 °C; CH_4/Ar = 1; GHSV = 3000 h^{-1}) are shown in Figure 1a and can be directly correlated with Mo K-edge XANES collected. The analysis of the position of the XANES absorption edge allows for identifying the Mo integer oxidation state thus following Mo reduction under CH_4. The oxidation states obtained from the edge position at different stages of reaction are shown in Figure 1b whilst the XANES spectra and the details of the analysis are described in Figure S3 and Table S1 in the ESI. During the first 7 minutes of reaction, a gradual decrease in the oxidation state was observed; i.e. from +6 down to ~ +4.1. MS traces in this period (see Figure S4 and corresponding discussion in ESI) show the typical evolution of combustion products (i.e. CO, CO_2 and H_2O) arising from the carburization of Mo. After 8 min, a further reduction of Mo was seen. Importantly, this was accompanied by the detection of aromatics by the MS, i.e. benzene and minor amounts of toluene, and an increase in the formation C_2H_x and C_3H_x hydrocarbons. After reaching a maximum after 20 min of reaction, the mass traces of CH_4 reactant rose in intensity while that of benzene steadily decreased, indicating the initiation of catalyst deactivation. The production of C_2H_x and C_3H_x in contrast, gradually increased, in agreement with previous reports.[25,35–37]

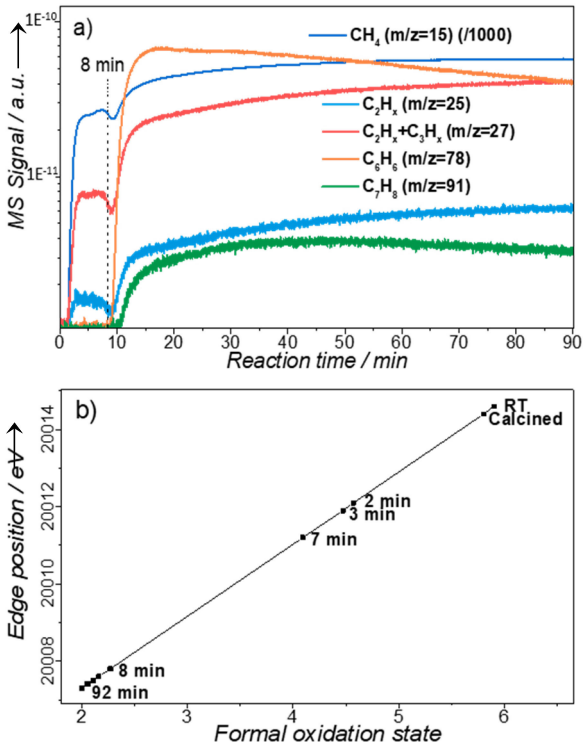

Figure 1. Data collected during the MDA reaction (T = 700 °C; CH_4/Ar = 1; GHSV = 3000 h^{-1}) on 3.8 w.% Mo/H-ZSM-5 (Si:Al = 15): a) MS traces for CH_4 and hydrocarbon products formed and b) Integer oxidation state of Mo species at different reaction times derived from the position of Mo K-edge.

Table 2. EXAFS fitting parameters for Mo/H-ZSM-5 during calcination, induction period and aromatization stages.[a]

Sample/ oxidation state	Shell	CN	R (Å)	σ^2 ($Å^2$)	E_0	R-factor
Calcined	Mo=O	2.0	1.69	0.00321	2.756	0.021
+5.8	Mo–O	2.0	1.85	0.00198		
2 min	Mo=O	0.6	1.69	0.00857	0.858	0.045
+4.6	Mo–O	2.0	1.85	0.02744		
	Mo–C	1.4	2.10	0.00211		
7 min	Mo=O	0.2	1.69	0.00183	−3.621	0.041
+4.1	Mo–O	1.8	1.85	0.02368		
	Mo–C	2.0	2.10	0.00179		
8 min	Mo–C	3.0	2.08	0.01374	−7.571	0.058
+2.3	Mo–Mo	1.6	2.95	0.01260		
90 min	Mo–C	3.0	2.08	0.01022	−7.706	0.030
+2.0	Mo–Mo	2.5	2.95	0.01260		

[a] Fitting Parameters: $S_0^2 = 0.82$, Fit Range: $3 < k < 12$, $1 < R < 4$, 16 independent parameters. Where N = Co-ordination number, R = Bond distance/ Å of the Absorber-Scatterer, σ^2 = Mean squared disorder term (sometimes referred to as the Debye Waller factor), $E_f = E_0$, R-Factor = A measure of the goodness of fit, which is a way of visualizing how the misfit is distributed over the fitting range. Note the high temperatures employed make it difficult the signal detection of the atoms in the second shell (i.e. Si and Al from the zeolite).

The accompanying radial distribution functions of the X-ray absorption fine structure (FT-EXAFS) spectra give insight into the distance and coordination number of nearest neighbor atoms. The FT-EXAFS at different stages of reaction (i.e. after calcination, during the induction period and subsequent aromatics formation) are plotted in Figure 2. As the experiment was carried out under dynamic conditions, it was not possible to unambiguously correlate one Mo environment with a particular EXAFS spectrum. However, what is clear from Figure 2 is that there are a number of distinctive peaks in the FTs that evolve under reaction conditions. The evolution of these peaks together with the integer oxidation states obtained serve as a guidance for the fitting of models to the real EXAFS data and the subsequent refinement of structure parameters. The resulting parameters are shown in Table 2 which correlate well with previously proposed Mo evolution; the experimental and simulated spectra are plotted in Figure S5.

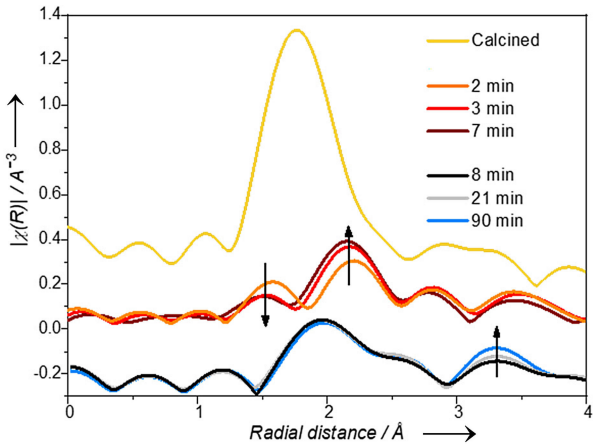

Figure 2. Mo K-edge FT-EXAFS spectra for 3.8 wt.% Mo/H-ZSM-5 at 8, 21 and 90 min of MDA reaction (50% CH_4/Ar, GHSV = 3000 h^{-1}, T = 700 °C)

Beginning with the monomeric Mo^{VI} in the calcined catalyst, the FT shown in Figure 2 exhibits a broad peak which can be approximated to a Mo^{VI} environment possessing Td symmetry i.e. coordinated to four oxygens at ~1.78 Å similar to those previously reported for Mo in reference compounds.[38] However, in order to achieve a charge neutral Mo^{VI} species in ZSM-5 it is necessary to consider a structure with two terminal Mo=O bonds at ~1.69 Å and two Mo–O bonds at ~1.85 Å (corresponding to framework oxygens). Although the k-range over which the EXAFS data are fitted is too low to clearly resolve two contributions from the same type of scatterer at similar distances, the two-shell refinement produced a sensible and stable fit (i.e. the two O shells do not converge to a single Mo–O distance). This is in agreement with previously proposed species where Mo-oxo species anchor to the zeolite BAS with tetrahedral coordination.[31] Further evidence for the validity of this approach is given in the ESI when comparing the FT from the calcined sample with the $Fe_2(MoO_4)_3$ reference and where it can be clearly seen that a shorter Mo–O radial distribution component is present in the Mo/H-ZSM-5 sample which is not present in the oxide reference where the Mo–O bonds lengths are uniformly longer at ~1.75 Å (Figure S6).[39]

Data recorded during the early stages of MDA (i.e. 2–7 min.) revealed a reduction in the FT intensities and the evolution of two distinct peaks. The shorter of the two components in the RDF corresponds to Mo=O whereas the longer distance corresponds well (based on bond length) to the presence of Mo–C. Using XANES-derived oxidation state information to limit the coordination state of the Mo species it is possible to propose that when Mo comes into contact with methane and after two minutes of reaction the number of short Mo=O terminal bonds decreases, i.e. are replaced by longer Mo–C bonds. We note however, that in order to obtain a good fit to the data it is necessary to include two Mo–O(framework) contributions at 1.85 Å although they are not obviously present on direct inspection of the FTs. Nevertheless, their inclusion in the simulation leads to an improvement in the fit even when taking into account the addition of extra parameters;[40] the comparatively large σ values for the Mo–O contribution is a consequence of destructive interference. With increasing reaction times (3 and 7 min.) in the induction period, the peak at longer radial distances (Mo–C) gradually increases at expense of the short distance peak (Mo=O). Interestingly it is this relative change in the respective contributions for Mo=O and Mo–C that also accounts for the apparent shift of the Mo–C peak in the FT to lower R values. This implies that reduction and carburization of Mo commences by replacement of terminal oxygens (as opposed to the longer and potential more labile single Mo–O bonds) by carbon forming new Mo–C bonds.

Above 8 min, the formal oxidation state of Mo is close to +2 and the spectra resembles closely the Mo_2C reference (see comparison in Figure S7 in the ESI). This suggests that also the bonds with framework oxygens have been replaced by carbon bonds, forming fully carburized Mo species. Furthermore, the presence of a new peak at c.a. 3.3 Å in the FT suggests the presence of heavy scatterers in the second shell, indicating formation of short-range ordered Mo carbide clusters (Mo–Mo distance of ~2.95 Å) from the initial isolated species. Taking the CNs obtained from the fits indicate, that on face value (i.e. not considering that the coordination numbers in EXAFS have an error associated with them typically between 10–20%), $Mo_{1.6}C_3$ clusters have formed. We note that at this point the induction period is complete and aromatic formation begins, evidencing that $Mo_{1.6}C_3$ clusters are the catalytically important species for methane dehydroaromatization. As proposed by some authors[23,41] the role of Mo_xC_y would be to promote the C–H bond dissociation in CH_4, leading to the formation of CH_x species that undergo dehydrogenation and C – C coupling resulting in C_2 intermediates. Previous Density Functional Theory (DFT) studies have suggested that the catalytic reactivity of Mo–C species can vary with the Mo:C ratio.[42,43] Since XAS is a bulk characterization technique and Mo/H-ZSM-5 is continuously evolving it is difficult to unambiguously differentiate between MoC species with varied Mo/C ratios which will likely present different activity. What can be clearly observed however, is that with further time on stream, a continuous intensity increase of the FT 3.3 Å peak occurs during MDA (bottom spectra in Figure 2). Average Mo CN increases from 1.6 to 2.5 in 90 min, pointing to a cluster growth during the course of reaction. This clustering can be attributed to detachment of Mo carbides from the zeolite framework making them susceptible to sinter.

High Resolution Powder Diffraction

Location of the Mo species in H-ZSM-5 was investigated by HRPD. Figure 3 shows the observed, calculated, and difference patterns obtained from Rietveld refinement (details of the refinement are given in Table S3 in the ESI whilst the experimental parameters and goodness-of-fit factors, coordinates, and selected bond distance can be found in Tables S4 to S7). The refined values of the unit and the framework refinement resulted in reasonable T–O bond length values, varying in the range of 1.52–1.80 Å, and T–O–T angles between 143° and 172°.[27]

Figure 4 presents the location of Mo determined by Difference Fourier mapping. For the calcined catalyst (Figure 4a), a large amount of electron density is located next to a particular framework position (designated Si(Al) 6), close to the wall of the straight channel and near the channel intersection. The brightness of this electron density cloud is consistent with a high Z element and is therefore assigned to Mo-containing species. The Mo–O average distances resulting from the refinement are 1.30(5) and 1.57(5) Å (Table S5). These distances are unphysically short showing the limitations of this technique for accurately resolving bond length, particularly when compared to EXAFS that is more suited to probing short-range order interactions.

Our PD data on reacted Mo/H-ZSM-5 show that Mo occupancy at the Si(Al) 6 position drastically decreases for the spent catalyst (i.e. ~70%, see tables S4 and S6 in the ESI) evidencing the migration of a significant fraction of Mo; consistent with previous theoretical calculations.[24] Further evidence for Mo detachment from the starting positions is given by NH_3-TPD which show a partial recovery of BAS after 90 min of reaction (see discussion in Figure S8 in ESI). Migration to the outer surface is

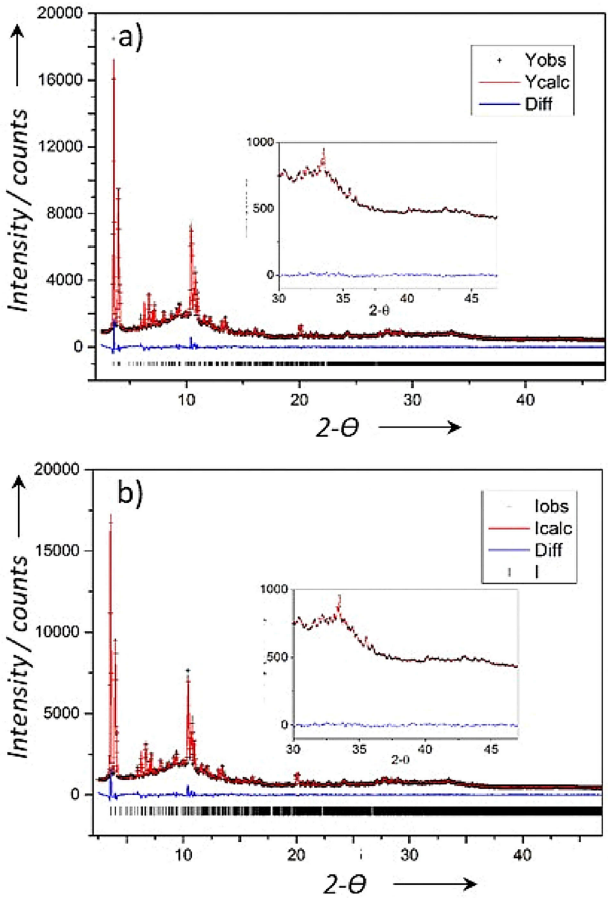

Figure 3. Rietveld plot for the diffraction for 3.8 wt.% Mo/H-ZSM-5: a) *in situ* calcined and b) *ex situ* reacted. The quality of fit at high angles are shown in the insets.

also suggested by transmission electron microscopy (TEM) images where of Mo-rich particles are seen to arise on the H-ZSM-5 crystal surface for the 90 min reacted catalyst (Figure S9). In addition, the Fourier map of the reacted sample (Figure 4b) shows very delocalized, weak electron clouds at the center of the zeolite channels, due to the presence of minor amounts of carbon deposits within the zeolite micropores.

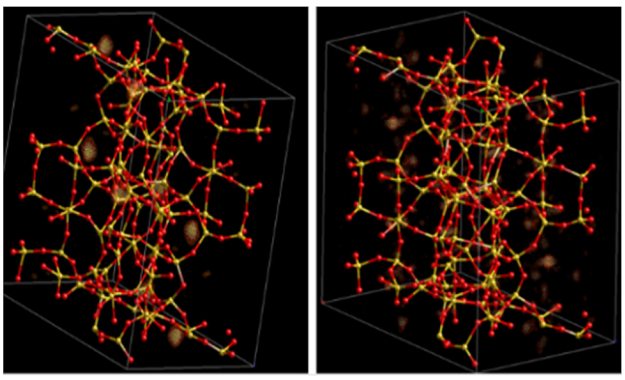

Figure 4. Crystal structure of 3.8 wt.% Mo/H-ZSM-5 (viewed along the b-axis) for the *in situ* calcined (a) and *ex situ* reacted (b) samples. Note the interlinked small yellow and red balls represent the zeolite framework. The larger diffuse spheres correspond to electron density assigned to Mo species (a) and C deposits (b).

Discussion

Figure 5 displays a schematic illustration of the structure and location of the evolving Mo species – as determined by combined *operando* XAFS and HRPD, together with the outlet products detected by MS at specific reaction times. Evaluation of the XAFS spectra with the subsequent EXAFS fittings confirms the previously proposed structures for Mo evolution on Mo/H-ZSM-5. This evolution commences with the formation of tetrahedral Mo-oxo species upon calcination comprising two terminal oxygens connected by double bonds and anchored to the zeolite through two bridging oxygens. HRPD reveals that such species appear predominantly anchored in a specific location within the H-ZSM-5 framework; i.e. in the straight channels near the channel intersections. This location is designated here as Si(Al) 6 (see Figure 5a for representation of the initial Mo-oxo species).

In contact with methane, during the induction period, the initial Mo-oxo species are reduced into partially carburized MoO_xC_y intermediate species. As this carburization commences by replacement of terminal oxygens by carbon, this partially carburized species are still attached to the Si(Al) 6 position of ZSM-5. Representation of the structure of these intermediates, refined by fitting of the EXAFS spectra, is shown in Figure 5b. The reaction product analysis carried out by MS show that at this stage CO, CO_2, H_2O and H_2 are formed while no aromatics are observed.

After 8 min reaction Mo is fully carburized; this complete carburization coincides with the first evidence of Mo agglomeration given by the increase in intensity of the peak 3.3 Å in the FT-EXAFS (Figure 5c), suggesting that Mo detaches from cation exchange positions to form small Mo_xC_y clusters. Importantly, these fully carburized Mo_xC_y species are the active species for the conversion of CH_4 to aromatics. This is consistent with previous research that has shown that bulk Mo_2C is active for aromatic production[37] and recent DFT calculations suggesting that small Mo carbide clusters promote coupling of CH_3 species.[44]

The EXAFS fittings indicate a gradual particle growth during the aromatization stage, from $Mo_{1.6}C_3$ at 8 min to $Mo_{2.5}C_3$ clusters after 90 min of reaction. With a maximum pore opening of ~5.6 Å it is clear that such clusters will be too large to fit into the pores of the ZSM-5 zeolite. Furthermore, according to previous literature, clusters with such C/Mo ratio are less stable inside the zeolite pores and thus expected to migrate to the zeolite outer surface.[24] As XAS only provides average CNs, we cannot rule out a wide cluster size distribution and the persistence of small clusters inside the pores. Our compelling evidence for the early Mo migration is in fact given by our HRPD data, showing around 70% decrease on Mo occupancy at Si(Al) 6 sites after 90 min. Mo migration outside the zeolite pores will limit the effect of the zeolite shape selectivity, as the absence of geometric constraints at the external surface will favor the formation of bulkier hydrocarbons, enhancing carbon deposition and triggering a fast catalyst deactivation. This correlates with our previous observations,[31] showing that significant carbon accumulation takes place on the external zeolite

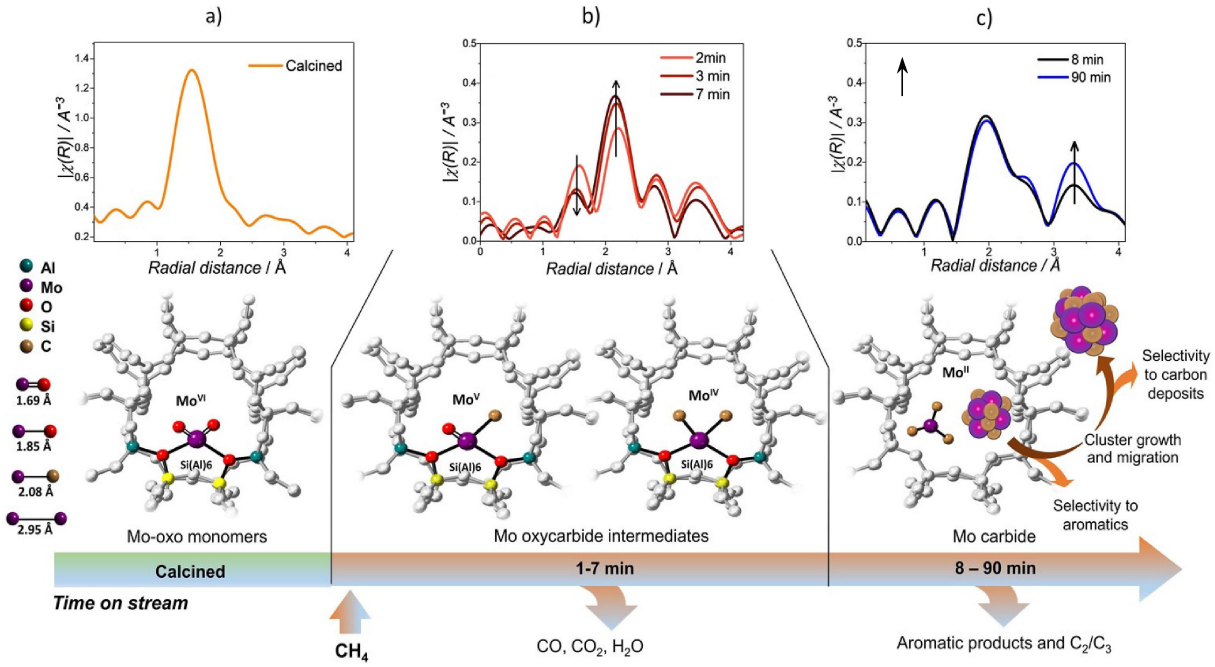

Figure 5. Schematic representation of Mo species evolution during MDA reaction on Mo/H-ZSM-5 catalyst as determined by operando XAS studies. The image shows the phase corrected FT-EXAFS spectra, the corresponding Mo species proposed, and the reaction products are pictured for the a) calcined sample, b) sample during the first 1-7 min of reaction (induction period) and c) sample between 8 to 92 min of reaction (aromatization stage).

surface, as well as with previous works reporting an increase in the rate in carbon deposition with time on stream.[12]

Summary and Conclusions

This study brings new insights into the structure and location of Mo species in Mo/H-ZSM-5 at each stage of the MDA process, enabling us to draw important conclusions regarding the deactivation mechanism. The key findings of this research are summarized as follows:

- *Operando* XAFS studies followed by EXAFS fittings support some of the previously proposed structures and observations for the evolution of Mo species under MDA conditions. Initial Mo-oxo species attached to the zeolite evolve to MoO_xC_y species during the induction period, with Mo=O bonds replaced before Mo–O (framework) bonds. However, these MoO_xC_y species do not yield any MDA products. Only when MoO_xC species are fully carburized to $Mo_{1.6}C_3$ are benzene, toluene etc. produced and allow us to conclude that these are the active species for dehydroaromatization.
- HRPD allows us to define the location of initial Mo-oxo species inside the zeolite pores. These appear anchored at a specific site close to the channel intersection. However, after 90 min of reaction the greater part of the Mo was seen to vacate the zeolite pores, migrating to the zeolite outer surface. These observations were supported by TEM measurements.
- The detachment of MoC_3 from the zeolite framework appears necessary for the formation of active, Mo_xC_y clusters. However, they are too unstable to remain housed within the zeolite micropores and this negatively affects product selectivity towards the desired MDA products (i.e. benzene). As such, a major cause of catalyst deactivation can be ascribed to a lack of product product shape-selectivity as a result of Mo migration, leading to coke build-up on the zeolite outer surface.

Importantly, our observations are also in line with recent studies showing that differences in Mo precursors or Al distribution have no influence on MDA catalytic behavior.[45] Although, calcination has been shown to regenerate and redistribute the Mo oxide species to create an active catalyst again,[21,46] up to date this approach cannot completely suppress deactivation. Accordingly, this study calls for a careful re-evaluation of synthesis strategies, with a change in focus towards stabilizing Mo carbides in a shape selective environment. For instance, by the use of different or secondary metals as the active species in MDA (i.e. Fe)[47] or by the addition of else promotors to the catalyst that could lead to less mobile active species.

Experimental Section

Catalyst Preparation and Characterization

ZSM-5 zeolite (Si:Al = 15) was supplied by Zeolyst International in the ammonium form (CBV3024E), and the H-form of the zeolite was obtained by calcination at 550 °C. Mo/H-ZSM-5 (4 wt.% Mo) was prepared by mixing H-ZSM-5 and MoO_3 (Sigma, 99.95%) powders in an agate mortar for 0.5 h. The physical mixture was then heated in air to 700 °C with a 5 °C/min ramp rate.

Ex situ catalytic reactions were carried out by introducing 0.6 g of catalyst (150–425 μm sieved fractions) into a tubular quartz rector. The internal diameter of the rector was 0.7 mm and catalyst bed

length was 3 cm. The sample was fixed in the isothermal zone of the oven by quartz wool. A total gas flow of 30 mL/min was fed by means of mass flow controllers which results in a gas hour space velocity (GHSV) of 1500 h^{-1}. The as-prepared physical mixtures (MoO_3 + support grinded in a mortar) were first activated under 20% O_2/He flow by heating up to 700 °C for 30 min using a ramp of 5 °C/min. After flowing 100% Ar for 30 min to flush the O_2 from the lines, methane dehydroaromatization was started by switching to a 50% CH_4/Ar flow. Products were analyzed by online mass spectrometer (OmniStar GSD 320O1).

Elemental analysis of the zeolites was carried out by inductively coupled plasma optical emission spectroscopy (ICP-OES) using a Perkin Elmer Optical Emission Spectrometer Optima 3300 RL.

Surface characterization of the zeolites was performed by nitrogen physisorption measured at 77.3 K on a Quadrasorb EVO QDS-30 instrument. The samples were outgassed at 350 °C overnight under high vacuum prior to the sorption. The Brunauer-Emmett-Teller equation was used to calculate the specific surface area in the pressure range $p/p_0 = 0.0006–0.01$. The micropore volume was calculated from the t-plot curve using the thickness range between 3.5 and 5.4 Å.

Thermogravimetric analysis measurements were carried out in a TA Q50 instrument. All samples were heated up to 950 °C using a ramp of 5 °C/min under an air flow of 60 mL/min; then they were held at 950 °C for 30 min.

X-ray diffraction patterns were recorded using a Rigaku SmartLab X-Ray Diffractometer fitted with a hemispherical analyzer. The measurements were performed using Cu Kα radiation source (λ = 1.5406 Å) with a voltage of 40 kV, and a current of 30 mA.

Fourier transform infra-red spectra were recorded in a Nicolet iS10 spectrometer. Samples were pressed into self-supporting wafers with a density ~10 mg/cm^2. The samples were dried prior the measurements by heating them up to 285 °C for 3 h under 70 ml/min He flow. After dehydration, the sample was cooled down to 150 °C under dry He for the spectra collection.

Temperature programmed desorption of ammonia (NH_3-TPD) measurements were performed in an AutoChem II 2920 Micromeritics instrument equipped with a moisture trap and a thermoconductivity detector. Samples were first preactivated by flowing pure N_2 and heating up to 550 °C for 30 min (5 °C/min). The reactor was then cooled down to 100 °C for ammonia absorption which was run by flowing 1% NH_3/N_2 until saturation (~1 h). Next, pure N_2 was flowed for 2 h to remove any excess of ammonia on the sample. Finally, ammonia desorption was carried out by increasing temperature up to 1100 °C with a ramp of 10 °C/min. All the signals were normalized to the sample mass.

Transmission electron microscopy measurements were performed using a JEM 2800 (Scanning) microscope. Voltage was 200 kV and the aperture 70 and 40 μm. Secondary electron signal was acquired providing topological information of the sample. Dark-field (Z-contrast) imaging in scanning mode was carried out using CCD detector and an off-axis annular detector.

High Resolution Powder Diffraction

High resolution powder diffraction (HRPD) data were collected at BM01 A beam line of the ESRF (the Swiss-Norwegian beamline). The diffractometer is based on a Huber goniometer with a Pilatus 2 M detector. X-rays with a wavelength of 0.69811 Å were used, selected by 2 Rh coated mirrors and a silicon (111) double crystal monochromator. The beamline setup is described in detail elsewhere.[48] Data were collected at a sample to detector distance of 260 mm – calibrated using NIST SRM660b lanthanum hexaboride – and a 2-θ range of 2 to 47° was used in the Rietveld analysis. Samples of as-prepared Mo/H-ZSM-5 were packed between plugs of quartz wool in 0.5 mm quartz capillaries and mounted in a Norby-type flow cell.[49] The samples were calcined by heating to a temperature of 600 °C with a heating rate of 6 °C/min and held for 8 h before cooling down to room temperature. A hot air blower was used to heat the sample and calcination was done under 10 mL/min flow of 20% oxygen in helium (GHSV = 750 h^{-1}). Data were collected with a collection time of 10 s per frame and converted to 1-D powder patterns using Fit2D[50,51] and the SNBL scaling software.[52] Data on *ex situ* reacted sample was also collected; the reaction was carried out at 700 °C for 90 min, using 50% CH_4/Ar flow (GHSV = 750 h^{-1}).

Rietveld and difference Fourier analysis was carried out with the TOPAS[53] software and the initial model for the framework was taken from the zeolite structure database; the MoO_3 model was taken from ICDD database. After refinement of the framework model to obtain reasonable lattice parameters, difference Fourier maps were used to locate the Mo atoms. The scaling factor was obtained using the high angle data which are not significantly affected by adsorption of molecules in a zeolite framework.[54] This was fixed for determination of the difference maps using the whole powder pattern. In the final Rietveld refinements all framework atom positions were refined without restrains along with isotropic thermal parameters for the silicon and oxygen atoms, background, peak broadening, scale factor, lattice parameters, zero point correction and occupancies for the non-framework atoms. The large electron density peak close to Si6 in the calcined sample was assigned to Mo, for the *ex situ* reacted sample three other sites were added as dummy carbon atoms to account for electron density due to carbonaceous coke in the framework.

X-ray Absorption Under *Operando* MDA

XAFS studies were performed at B18 beamline at Diamond Light Source in Harwell, United Kingdom. The electron energy was 3 GeV and the ring current 300 mA. Mo K-edge XAFS measurements (in the range of 19,797 to 21,000 eV) were recorded in transmission mode using ion chamber detectors with a fast scanning Si (111) double crystal monochromator. The acquisition of each spectra took ~60 s, with a Mo foil placed between It and Iref. The dimensions of the X-ray beam used were 1 × 1 mm^2. XAS data analysis was performed using the Demeter software package.[55] For all the fittings the amplitude and coordination numbers were set. The value of amplitude, 0.91, was obtained by fitting the Mo foil reference to crystallographic data form ICSD database.

For the MDA operando experiments, 40 mg of the as-prepared catalyst (sieve fractions: 0.425–0.150 mm) were placed within a 3 mm diameter quartz capillary, and calcined at 700 °C for 30 min (20% O_2 in He). The sample heating was carried out by a hot air blower. Keeping the temperature at 700 °C, the lines were flushed with Ar for 15 min to remove O_2. Then, the flowing gas was switched to a CH_4/Ar mixture (1:1) and the MDA reaction was carried out for 90 min (at 700 °C, GHSV = 3000 h^{-1}).

Catalytic data were recorded using an online mass spectrometer (OmniStar GSD 320O1) connected to the capillary outlet. The reactor outlet was connected to the MS by heated lines at 200 °C to avoid condensation of products. For mass spectrometry results, T = 0 for the MDA reaction was taken as the time where CH_4 signal (m/z = 15) rise was first detected.

The spectra acquisition time (60 s) as well as the dead volume between the Mass Flow Controller (MFC) and the reactor (i.e. time

needed for the gas to reach the reactor) were considered for the correlation of MDA reaction time and XAS data collection times.

Mo_2C, MoO_3 and $Fe_2(MoO_4)_3$ references were also measured; these were purchased from Sigma Aldrich (purity > 99.5 %). The reference spectra were collected in pellet form (300 mg sample in 1.3 mm diameter pellet) at room temperature. Samples were first diluted with cellulose aiming for an adsorption step $mx = \sim 1$ (being m the atomic absorption coefficient in cm^{-1} and x is the thickness in cm).

Acknowledgements

This study received financial support from a UCL Impact PhD award, Diamond Light Source and Johnson Matthey Plc. Diego Gianolio and Dimitri Chernyshov are kindly acknowledged for assistance during DLS and ESRF beamtimes respectively. Johnson Matthey is thanked for the chemical analysis and TEM measurements. This research used resources from RCaH. EPSRC is also acknowledged for sponsoring the UK Catalysis Hub which provided resources and support via grants EP/K014706/1, EP/K014668/1, EP/K014854/1, EP/K014714/1 and EP/I019693/1 and for an Early Career Fellowship for AMB (EP/K007467/1).

Conflict of Interest

The authors declare no conflict of interest.

Keywords: MDA · Mo-ZSM-5 · operando · XAFS · HRPD

[1] J. N. Armor, *J. Energy Chem.* **2013**, *22*, 21–26.
[2] P. Tang, Q. Zhu, Z. Wu, D. Ma, *Energy Environ. Sci.* **2014**, *7*, 2580–2591.
[3] B. M. Weckhuysen, D. Wang, M. P. Rosynek, J. H. Lunsford, *J. Catal.* **1998**, *175*, 347–351.
[4] S. Ma, X. Guo, L. Zhao, S. Scott, X. Bao, *J. Energy Chem.* **2013**, *22*, 1–20.
[5] J. J. Spivey, G. Hutchings, *Chem. Soc. Rev.* **2014**, *43*, 792–803.
[6] Z. R. Ismagilov, E. V. Matus, L. T. Tsikoza, *Energy Environ. Sci.* **2008**, *1*, 526–541.
[7] B. M. Weckhuysen, M. P. Rosynek, J. H. Lunsford, *Catal. Lett.* **1998**, *52*, 31–36.
[8] J. Shu, A. Adnot, B. P. A. Grandjean, *Ind. Eng. Chem. Res.* **1999**, *38*, 3860–3867.
[9] C. H. L. Tempelman, E. J. M. Hensen, *Appl. Catal. B* **2015**, *176*, 731–739.
[10] V. I. Zaikovskii, A. V Vosmerikov, V. F. Anufrienko, L. L. Korobitsyna, E. G. Kodenev, G. V Echevskii, N. T. Vasenin, S. P. Zhuravkov, E. V Matus, Z. R. Ismagilov, V. N. Parmon, *Kinet. Catal.* **2006**, *47*, 389–394.
[11] E. V. Matus, I. Z. Ismagilov, O. B. Sukhova, V. I. Zaikovskii, L. T. Tsikoza, Z. R. Ismagilov, J. A. Moulijn, *Ind. Eng. Chem. Res.* **2007**, *46*, 4063–4074.
[12] J. Bai, S. Liu, S. Xie, L. Xu, L. Lin, *Catal. Lett.* **2003**, *90*, 123–130.
[13] T. Behrsing, H. Jaeger, J. V. Sanders, *Appl. Catal.* **1989**, *54*, 289–302.
[14] J. Bai, S. Liu, S. Xie, L. Xu, L. Lin, *Catal. Lett.* **2004**, *82*, 279–286.
[15] D. Ma, Y. Shu, X. Han, X. Liu, Y. Xu, X. Bao, *J. Phys. Chem.* **2001**, *105*, 1786–1799.
[16] H. S. Lacheen, E. Iglesia, *Phys. Chem. Chem. Phys.* **2005**, *7*, 538–547.
[17] Y. H. Kim, R. W. Borry, E. Iglesia, *Microporous Mesoporous Mater.* **2000**, *35*, 495–509.
[18] H. Ma, R. Kojima, R. Ohnishi, M. Ichikawa, *Appl. Catal. A* **2004**, *275*, 183–187.
[19] N. Kosinov, F. J. A. G. Coumans, G. Li, E. Uslamin, B. Mezari, A. S. G. Wijpkema, E. A. Pidko, E. J. M. Hensen, *J. Catal.* **2017**, *346*, 125–133.
[20] N. Kosinov, F. J. A. G. Coumans, E. Uslamin, F. Kapteijn, E. J. M. Hensen, *Angew. Chem. Int. Ed.* **2016**, *55*, 15086–15090; *Angew. Chem.* **2016**, *128*, 15310–15314.
[21] M. T. Portilla, F. J. Llopis, C. Martínez, *Catal. Sci. Technol.* **2015**, *5*, 3806–3821.
[22] S. H. Morejudo, R. Zanón, S. Escolástico, I. Yuste-Tirados, H. Malerød-Fjeld, P. K. Vestre, W. G. Coors, A. Martínez, T. Norby, J. M. Serra, C. Kjølseth, *Science (80-.).* **2016**, *353*, 563–566.
[23] W. Ding, S. Li, G. D. Meitzner, E. Iglesia, *J. Phys. Chem. B* **2001**, *105*, 506–513.
[24] J. Gao, Y. Zheng, G. B. Fitzgerald, J. de Joannis, Y. Tang, I. E. Wachs, S. G. Podkolzin, *J. Phys. Chem. C* **2014**, *118*, 4670–4679.
[25] R. W. Borry, Y. H. Kim, A. Huffsmith, J. a. Reimer, E. Iglesia, *J. Phys. Chem. B* **1999**, *103*, 5787–5796.
[26] W. Li, G. D. Meitzner, R. W. Borry, E. Iglesia, *J. Catal.* **2000**, *191*, 373–383.
[27] B. Li, S. Li, N. Li, H. Chen, W. Zhang, X. Bao, B. Lin, *Microporous Mesoporous Mater.* **2006**, *88*, 244–253.
[28] J. P. Tessonnier, B. Louis, S. Rigolet, M. J. Ledoux, C. Pham-Huu, *Appl. Catal. A* **2008**, *336*, 79–88.
[29] J. Gao, Y. Zheng, J.-M. Jehng, Y. Tang, I. E. Wachs, S. G. Podkolzin, *Science (80-.).* **2015**, *348*, 686–690.
[30] J. P. Tessonnier, B. Louis, S. Walspurger, J. Sommer, M. J. Ledoux, C. Pham-Huu, *J. Phys. Chem. B* **2006**, *110*, 10390–10395.
[31] I. Lezcano-González, R. Oord, M. Rovezzi, P. Glatzel, S. W. Botchway, B. M. Weckhuysen, A. M. Beale, *Angew. Chem. Int. Ed.* **2016**, *55*, 5215–5219; *Angew. Chem.* **2016**, *128*, 5301–5305.
[32] D. Wang, J. H. Lunsford, M. P. Rosynek, *J. Catal.* **1997**, *358*, 347–358.
[33] D. Ma, Y. Shu, X. Bao, Y. Xu, *J. Catal.* **2000**, *189*, 314–325.
[34] S. E. Shadle, B. Hedman, K. Hodgson, E. I. Solomon, *Inorg. Chem.* **1994**, *33*, 4235–4244.
[35] C. H. L. Tempelman, X. Zhu, E. J. M. Hensen, *Chinese J. Catal.* **2015**, *36*, 829–837.
[36] S. Liu, L. Wang, R. Ohnishi, M. Ichikawa, *J. Catal.* **1999**, *181*, 175–188.
[37] F. Solymosi, J. Cserényi, A. Szöke, T. Bánsági, A. Oszkó, *J. Catal.* **1997**, *165*, 150–161.
[38] G. Plazenet, E. Payen, J. Lynch, B. Rebours, *J. Phys. Chem. B* **2002**, *106*, 7013–7028.
[39] A. M. Beale, S. D. M. Jacques, E. Sacaliuc-Parvalescu, M. G. O'Brien, P. Barnes, B. M. Weckhuysen, *Appl. Catal. A* **2009**, *363*, 143–152.
[40] D. C. Koningsberger, B. L. Mojet, G. E. Van Dorssen, D. E. Ramaker, *Top. Catal.* **2000**, *10*, 143–155.
[41] D. Zhou, S. Zuo, S. Xing, *J. Phys. Chem.* **2012**, *116*, 4060–4070.
[42] P. Liu, J. A. Rodriguez, *J. Chem. Phys.* **2004**, *120*, 5414–5423.
[43] C. Jimenez-Orozco, E. Florez, A. Moreno, P. Liu, J. J. Rodriguez, *J. Phys. Chem.* **2017**, *121*, 19786–19795.
[44] T. S. Khan, S. Balyan, S. Mishra, K. K. Pant, M. A. Haider, *J. Phys. Chem. C*, DOI:10.1021/acs.jpcc.7b09275.
[45] I. Vollmer, G. Li, I. Yarulina, N. Kosinov, E. J. Hensen, K. Houben, D. Mance, M. Baldus, J. Gascon, F. Kapteijn, *Catal. Sci. Technol.* **2018**, *8*, 916–922.
[46] N. Kosinov, F. J. A. G. Coumans, E. Uslamin, F. Kapteijn, E. J. M. Hensen, *Angew. Chem. Int. Ed.* **2016**, *55*, 15086–15090; *Angew. Chem.* **2016**, *128*, 15310–15314.
[47] X. Guo, G. Fang, G. Li, H. Ma, H. Fan, L. Yu, C. Ma, X. Wu, D. Deng, M. Wei, D. Tan, R. Si, S. Zhang, J. Li, L. Sun, Z. Tang, X. Pan, X. Bao, *Science* **2014**, *344*, 626–629.
[48] BM01 ESRF, http://www.esrf.eu/UsersAndScience/Experiments/CRG/BM01/bm01-a.
[49] P. Norby, *Mater. Sci. Forum* **1996**, *228*, 147–152.
[50] http://pubs.acs.org/doi/pdf/10.1021/acs.jpcc.5b06875.
[51] A. P. Hammersley, S. O. Svensson, M. Hanfland, A. N. Fitch, D. Hausermann, *High Press. Res.* **1996**, *14*, 235–248.
[52] http://www.esrf.eu/home/UsersAndScience/Experiments/CRG/BM01
[53] A. A. Coelho, *TOPAS V4.1*, *Bruker AXS*, **2006**.
[54] L. B. McCusker, R. B. Von Dreele, D. E. Cox, D. Louër, P. Scardi, IUCr, *J. Appl. Crystallogr.* **1999**, *32*, 36–50.
[55] B. Ravel, M. Newville, *J. Synchrotron Radiat.* **2005**, *12*, 537–541.

Manuscript received: August 9, 2018
Accepted manuscript online: September 11, 2018
Version of record online: October 5, 2018

FULL PAPERS

Mission Operando: *Operando* XAS and HRPD/difference Fourier mapping enable the determination of the structure and location of evolving Mo species on H-ZSM-5 during methane dehydroaromatization, demonstrating their influence on product distribution and defining Mo_xC_y as the active species. The instability and migration of these active species to the zeolite outer surface is a major cause of catalyst deactivation.